Plasmonics (2018) 13:1615–1621
https://doi.org/10.1007/s11468-017-0670-6

Propagation Properties of Nanoscale Three-Dimensional Plasmonic Waveguide Based on Hybrid of Two Fundamental Planar Optical Metal Waveguides

Wenjin Wang[1] · Huimin Ye[1] · Qian Wang[1,2] · Weihua Lin[1]

Received: 15 September 2017 / Accepted: 14 November 2017 / Published online: 28 November 2017

Abstract
In this paper, a nanoscale three-dimensional plasmonic waveguide (TDPW), created by depositing an Ag stripe on a SiO_2 layer with an Ag substrate, is introduced and theoretically investigated at visible and telecom wavelengths. By applying the effective index method and finite-difference time-domain numerical simulations, the authors find that the propagation properties of surface plasmon polaritons (SPPs) in the TDPW, including the propagation length and beam width, are mainly decided by the core (the SiO_2 layer just under the Ag stripe) itself, due to the much stronger localization of SPPs in the core than in the two side claddings (the SiO_2 layer without the covered Ag stripe). And propagating SPPs in the TDPW are strongly confined in the core region, even with a very small waveguide cross section. Furthermore, based on the stronger localization of propagation SPPs in the TDPW, two kinds of bending waveguides, oblique bending and 90° circular bending waveguides, are also investigated. For wavelength of 1550 nm, the 90° circular bending guide with a minimum radius as small as 2.6 μm show nearly zero radiation loss, even with a small waveguide cross section of 70×80 nm^2. The proposed TDPW is suitable for planar integration and provides a possible way for constructing various nanoscale counterparts of conventional integrated devices such as splitter, resonator, sensor, and optical switch.

Keywords Surface plasmon polaritons · Nanoscale optical waveguide · Photonic integrated circuits · Finite-difference time-domain

Introduction

The demands of giant information processing stimulate the processing circuits to have ultrahigh data transfer speed simultaneously with extra small size. Conventional integrated optical devices have raised considerable interests in the race to overcome data transfer limitation in electronic circuits for their high bandwidth; however, they are difficulties to be scaled down to nanoscale due to the light diffraction limit. As an evanescent electromagnetic wave propagating along the interface of metallo-dielectrics, surface plasmon polaritons (SPPs), quantized hybrid modes derived from the resonant interaction between exciting photons and surface electrons of metal, are considered to possess the advantages of photons and electrons. SPPs not only show the capability of overcoming the diffraction limit, but also can localize light energy in a nanoscale domain, and thus are regarded as a representative information carrier for next-generation integrated nanophotonic devices [1–3].

Currently, tremendous efforts are being devoted to develop SPPs-based nano waveguide and circuits including chains of metal nanoparticles [4], metal nanowires/stripes [5, 6], metal gap waveguides [7–9], trench/slot waveguides in metal thin films [10, 11], metal heterostructure [12–15], low-index core of metal-dielectric waveguides [16], V-shaped/wedge metal waveguides [17–20], and hybrid type V-shaped/wedge metal waveguides [21]. Practically, the application of the waveguides should consider the trade-off between propagation loss, field confinement, structure dimensions, and fabrication. Recently, a plasmonic structure by depositing a dielectric stripe on a metal surface, called dielectric-loaded SPPs waveguide [22–24], is proposed. On the one hand, the waveguide is

✉ Weihua Lin
linwh_whu@hotmail.com

[1] Key Laboratory of Artificial Micro- and Nano-structures of Ministry of Education and School of Physics and Technology, Wuhan University, Wuhan 430072, China

[2] Department of Physics, Wenhua College, Wuhan 430074, China

suitable for planar integration; on the other hand, it can solve the problem on the increased light scattering with the diminishingly metal stripe edges, which is met in metal stripe waveguide, but the dimension of dielectric stripe perpendicular to SPPs propagation direction still cannot be decreased any more. Furthermore, hybrid dielectric-loaded SPP waveguides [25–31] were proposed, such as a structure by depositing a high refractive index media stripe on the low refractive index stripe of dielectric-loaded SPP waveguide [26]. The waveguide shows possessing a large propagation length, and the light seems to be squeezed into the low index dielectric stripe within a very small structure cross section, but in fact, the field still extends into the high index layer.

In this paper, a nanoscale three-dimensional plasmonic waveguide (TDPW) with sample structure is proposed by depositing a metal stripe on a dielectric film with a metal substrate. The waveguide can be viewed as a hybrid of two fundamental of planar plasmonic waveguides and is suitable for planar integration. The SPP propagation properties in the straight TDPW are investigated by carrying out the effective index method (EIM) and the finite-different time-domain (FDTD) method, and the waveguide shows that it can strongly confine propagating SPPs in the core area even with a very small waveguide cross section. In addition, oblique bending and 90° circular bending waveguides structured with the TDPW are also investigated, and a 90° circular bending waveguide for wavelength of 1550 nm with a radius as small as 2.6 μm shows nearly zero radiative loss. The rest of this paper is organized as follows. In the "Design and Theoretical Analysis" section, the geometric model of the TDPW and theoretical analysis of SPP propagation properties in the TDPW calculated by EIM are presented. In the "Numerical Simulations and Discussions" section, numerical results of SPPs propagating in the TDPW by FDTD, as well as the transmission properties of two kinds of bending waveguides, are displayed, and some discussions based on the EIM results and FDTD results are also presented. Finally, conclusions are drawn in the "Conclusions" section.

Design and Theoretical Analysis

The considered two fundamental planar plasmonic waveguides (infinite along y axis), shown in Fig. 1a, are metal-dielectric-metal waveguide (MDMW) and metal-dielectric-air waveguide (MDAW). One can get the complex propagation constant $\beta(=\beta_R + i\beta_I)$ of SPPs in the MDMW and MDAW by solving the dispersion equations [32]:

$$\frac{\varepsilon_d q}{\varepsilon_m k_d} = \frac{1-e^{k_d t_d}}{1+e^{k_d t_d}} \tag{1}$$

and

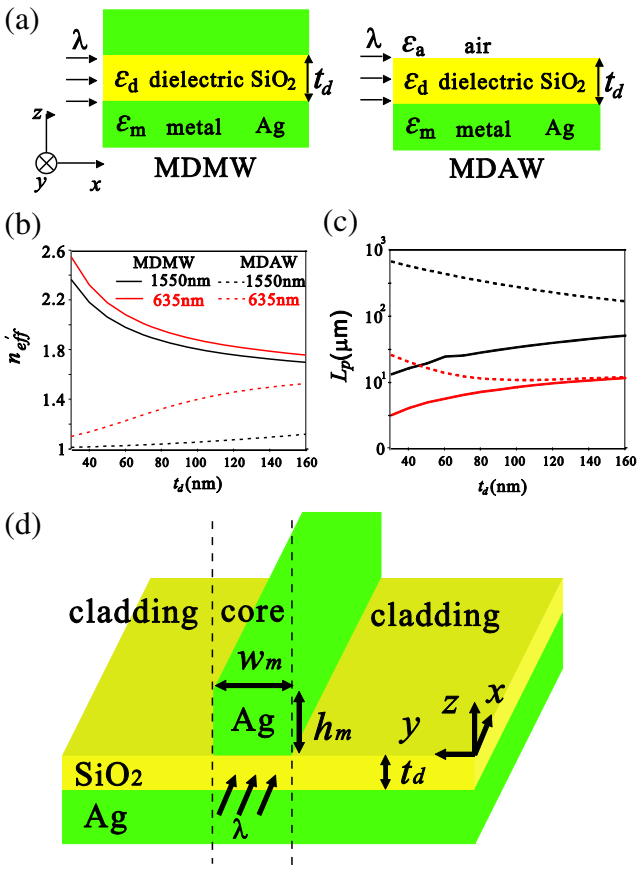

Fig. 1 **a** Schematics of MDMW and MDAW. Dependence of **b** n_{eff}' and **c** L_p of MDMW (solid curve) and MDAW (dashed curve) on the thickness of dielectric layer t_d for wavelength of 635 nm (red) and 1550 nm (black). **d** Three-dimensional schematic of the TDPW (color figure online)

$$k_d t_d = \tan^{-1}\left(\frac{\varepsilon_d p}{\varepsilon_a k_d}\right) + \tan^{-1}\left(\frac{\varepsilon_d q}{\varepsilon_m k_d}\right) \tag{2}$$

respectively, with $k_d = \left(k_0^2\varepsilon_d - \beta^2\right)^{1/2}$, $p = \left(\beta^2 - k_0^2\varepsilon_a\right)^{1/2}$, and $q = \left(\beta^2 - k_0^2\varepsilon_m\right)^{1/2}$, where ε_m,ε_d,$\varepsilon_a$are the permittivities of metal, dielectric, and air, respectively. t_d is the thickness of the dielectric layer, and k_0 presents the wave vector of the incident light in vacuum. The effective refractive index (n_{eff}) of the electromagnetic mode in the waveguides can be defined as $n_{eff} = n_{eff}' + in_{eff}'' = \beta/k_0$, and the corresponding propagation length (L_p) is obtained from $L_p = \lambda/(4\pi n_{eff}'')$; here λ is the wavelength of incident light. As the metal and dielectric are chosen as silver and SiO_2 (with a constant permittivity of ε_d = 2.25), Fig. 1b, c shows the dependence of n_{eff}' and L_p on t_d, respectively, for two wavelengths of 635 and 1550 nm, as the permittivities of Ag, fitting data from [33], are $\varepsilon_m = -18.4 + 0.5i$ (λ=635 nm) and $\varepsilon_m = -129.6 + 3.2i$ (λ=1550 nm).

From Fig. 1b, it can be clearly noticed that n_{eff}' of MDMW and MDAW decreases and increases, respectively, with the increase of t_d; moreover, the former is always larger than the latter with the same t_d and λ, but the difference of n_{eff}' between

MDMW and MDAW reduces with the increase of t_d. As shown in Fig. 1c, the L_p of SPPs in MDAW and in MDMW reduces and increases, respectively, with the increase of t_d. And the L_p of SPPs in MDAW is always larger than that in MDMW with the same t_d and λ, but the difference between them will reduce to zero as t_d increases to be a large value. It is well known that light tends to spread with a lower velocity at which the effective index is higher. According to this fact, a nanoscale TDPW, shown in Fig. 1d, is proposed just by depositing a Ag stripe on a MDAW. The core of the TDPW is the region from bottom to top covered with the Ag stripe, which, in fact, can be seen as a MDMW with finite size in the y direction, and the two side claddings of the TDPW are regions without Ag stripe cover. The thickness of the SiO_2 layer and the width and height of the Ag stripe are three important geometry parameters of the TDPW, donated as t_d, w_m, and h_m, respectively, as shown in Fig. 1d. SPPs in the TDPW are expected to propagate along the SiO_2 region just under the Ag stripe along the x direction.

A theoretical analysis of the SPP propagation properties in the TDPW is made by EIM, of which the TDPW is treated as a three-layer symmetry dielectric planar waveguide. And the n_{eff} of the core and claddings needed in the EIM analysis is acquired from those of MDMW and MDAW, respectively. Figure 2 illustrates the EIM results of the dependence of the n_{eff}', L_p, and beam width (w_b) of SPPs in the TDPW on t_d and w_m as h_m is large enough (> 1 μm). From Fig. 2a, b, one can observe that the n_{eff}' of SPPs in the TDPW decreases at first and then increases slowly with the increase of t_d as w_m is fixed for both wavelengths, and when t_d is fixed, it gradually increases with the increase of w_m. For $\lambda = 635$ nm, as shown in Fig. 2c, the L_p of SPPs in the TDPW undergoes a gradual increase with the increase of t_d with a fixed w_m; however, for $\lambda = 1550$ nm, L_p also shows a gradual increase with the increase of t_d as w_m is fixed to a value larger than 100 nm (shown in Fig. 2d), but undergoes an increase at first and then decreases with the increase of t_d when w_m is fixed to a value smaller than 100 nm. And, as w_m is fixed, the w_b of SPPs in the TDPW also gradually increases with the increase of t_d for both wavelengths. On the other hand, when t_d is fixed, L_p and w_b both gradually reduce with the increase of w_m for both wavelengths. For $\lambda = 635$ nm, the maximum and minimum L_p are 11.0 and 3.3 μm with waveguide cross sections of 120 × 30 nm^2 (namely, $t_d = 120$ and $w_m = 30$ nm; the format is suitable for all below) and 30 × 100 nm^2, respectively. And for $\lambda = 1550$ nm, the maximum and minimum L_p are 256.0 and 15.4 μm with waveguide cross sections of 70 × 30 and 30 × 200 nm^2, respectively. The minimum w_b of the EIM results is 0.15 and 0.37 μm for $\lambda = 635$ and 1550 nm, with waveguide cross sections of 30 × 90 and 30 × 200 nm^2, respectively.

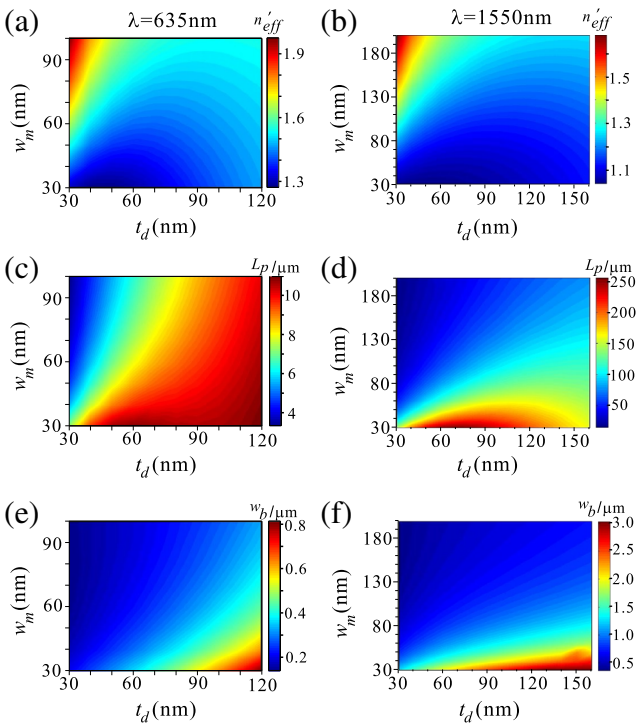

Fig. 2 EIM results of dependence of **a**, **b** n_{eff}', **c**, **d** L_p, and **e**, **f** w_b of propagating SPPs in the TDPW on t_d and w_m. **a**, **c**, **e** $\lambda = 635$ nm. **b**, **d**, **f** 1550 nm (color figure online)

Numerical Simulations and Discussions

Following the EIM analysis, FDTD numerical simulations is applied to depict the electric field distribution of SPPs propagating in the TDPW. In the FDTD simulations, the size of cells in the x, y, and z directions are set as $\Delta x = \Delta y = \Delta z = 10$ nm, and the time step is set as $\Delta t = \Delta x/2c$, where c is the velocity of light in vacuum. A Gaussian TM-polarized wave with magnetic field parallel to the y axis (see Fig. 1d) is illuminated on the input end of the TDPW along the positive x axis, and the beam width of incident light is set to be larger than the width of the Ag stripe.

Since the Ag stripe with a large h_m is not suitable for nanofabrication processing, the influence of h_m on SPP propagation properties in the TDPW is then firstly investigated in FDTD simulations. The FDTD results of the dependence of L_p of SPPs in the TDPW on h_m are shown in Fig. 3a, b for $\lambda =$ 635 nm (with waveguide cross section of 70 × 60 nm^2) and 1550 nm (with waveguide cross section of 70 × 80 nm^2), respectively. One can observe that L_p increases with h_m and becomes stable as h_m is larger than 90 nm for $\lambda = 635$ nm (see Fig. 3a). And L_p increases to saturation as h_m is larger than 200 nm for $\lambda = 1550$ nm (see Fig. 3b).

Based on the results shown in Fig. 3a, b, the h_m of TDPW for $\lambda = 635$ and 1550 nm are fixed to 90 and 200 nm, respectively, for all the simulation work below. Figure 3c, d shows the dependence of L_p and w_b on t_d and w_m, respectively, for $\lambda = 635$ nm. Corresponding results for $\lambda = 1550$ nm are

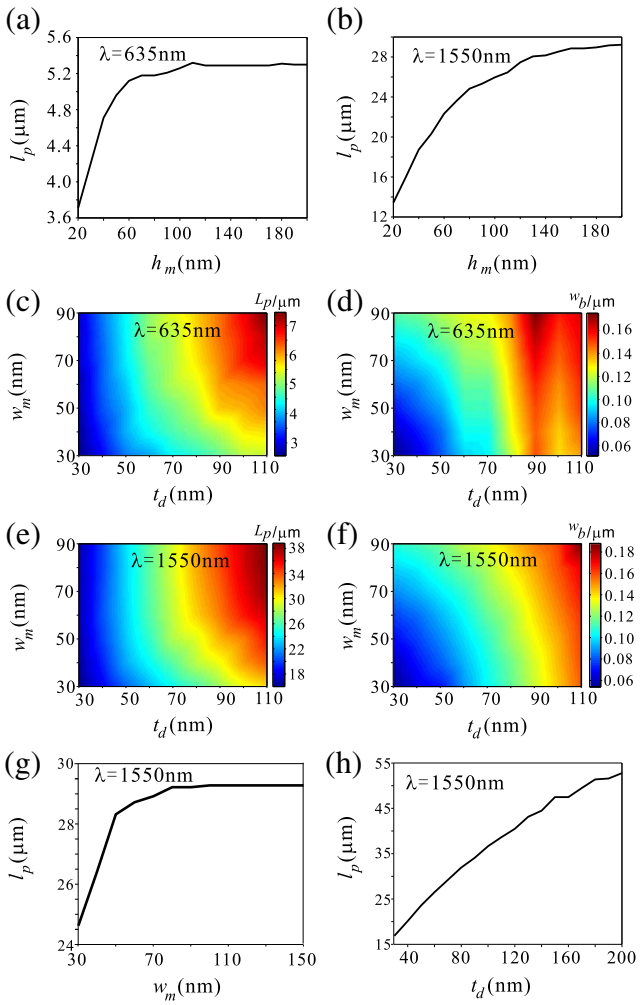

Fig. 3 FDTD results of the dependence of L_p of propagation SPPs in the TDPW on h_m **a** for $\lambda = 635$ nm (with a waveguide cross section of 70 × 60 nm^2) and **b** for 1550 nm (with a waveguide cross section of 70 × 80 nm^2). Dependence of **c**, **e** L_p and **d**, **f** w_b of propagating SPPs in the TDPW on t_d and w_m. **c**, **d** $\lambda = 635$ nm (with fixed $h_m = 90$ nm). **e**, **f** 1550 nm (with fixed $h_m = 200$ nm). Dependence of L_p of propagating SPPs in the TDPW **g** onw_m with t_d fixed at 70 nm and **h** on t_d with w_m fixed at 80 nm, for 1550 nm (color figure online)

displayed in Fig. 3e, f, respectively. FDTD simulation results show that L_p and w_b both increase with t_d when w_m is fixed, which accords with the results of EIM. Since the larger the t_d, the smaller the ohmic loss of the core of the TDPW (see Fig. 1c), and simultaneously, the smaller the difference of n_{eff}' between the core and the two side claddings (see Fig. 1b), the lower the confinement of SPPs in the core; as a result, L_p and w_b both ascend with t_d. Therefore, when w_m is fixed, the results of FDTD and EIM, regarding the dependence of the L_p and w_b on t_d, accord with each other.

When t_d is fixed, FDTD results show that L_p and w_b also both increase slightly with w_m; however, the result shows a discrepancy with the EIM results as shown in Fig. 2. Furthermore, one can also find that the values of L_p and w_b based on FDTD are much smaller than those of corresponding EIM results, and the maximum L_p in the TDPW of FDTD result is close to that in the MDMW with the same t_d. For example, the L_p and w_m of FDTD results are 29 μm and 130 nm (with the FDTD-simulated electric field [$|E|^2$] distributions in the *yz* and *xy* plane shown in Fig. 4c, d), respectively, while those of the EIM results are 96 μm and 886 nm, for $\lambda = 1550$ nm and with waveguide cross section of 70 × 80 nm^2. And for $\lambda = 635$nm, as waveguide cross section is 70 × 60 nm^2, the L_p and w_m of FDTD results are 5.21 μm and 108 nm (with the FDTD simulated $|E|^2$ distributions in the *yz* and *xy* plane shown in Fig. 4a, b), respectively, while those of the EIM results are 8.6 μm and 254 nm, respectively. As mentioned in the "Design and Theoretical Analysis" section, the TDPW is treated as a three-layer symmetry dielectric planar waveguide in the EIM analysis. In view of the three-layer dielectric waveguide, the larger the width of the core

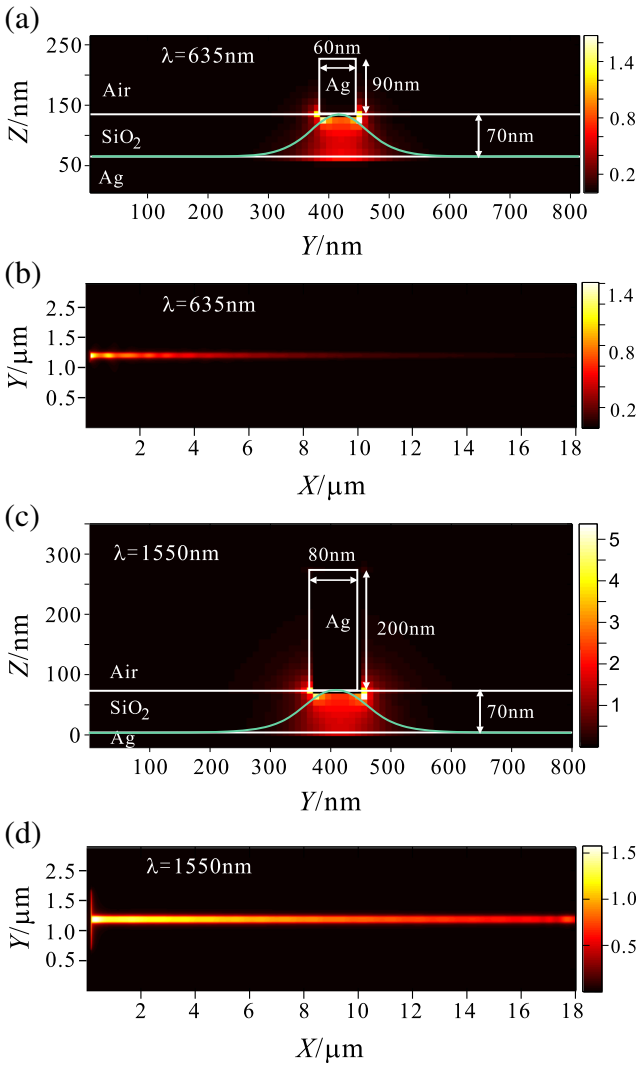

Fig. 4 FDTD-simulated electric field ($|E|^2$) distributions in the **a**, **c** *yz* and **b**, **d** *xy* plane. **a**, **b** $\lambda = 635$ nm, with a waveguide cross section of 70 × 60 nm^2 (namely, $t_d = 70$ nm and $w_m = 60$ nm). **c**, **d** $\lambda = 1550$ nm with a waveguide cross section of 70 × 80 nm^2 (color figure online)

layer (namely, the w_m), the stronger the confinement of light in the core, and thus the smaller the w_b; furthermore, the smaller the L_p in the EIM analysis (see Fig. 2) due to the fact that the ohmic loss of the core is higher than that of the two side claddings (see Fig. 1c). However, there is a weakness in the EIM analysis that EIM neglects the fact that the localization of electromagnetic field in the MDMW is much stronger than that in MDAW. Due to the much stronger localization of SPPs in MDMW, the SPP is strongly confined in the core of TDPW (which can be regarded as a MDMW with finite size in the y direction, see Fig. 1d) and only expending a very small distance into the cladding layer (one can clearly see from the field distributions in Fig. 4); thus, the w_b of FDTD results is much smaller than that of EIM results. Also, the w_b of FDTD results increases with the increase of w_m, instead of reducing with the increase of w_m (EIM results). The phenomenon that the w_b of FDTD results is smaller than that of EIM results is also shown in planar hetero-metal waveguides [13], which is attributed to the fact that EIM neglects the stronger localization of electromagnetic field on the Ag surface than that on the Al surface. Furthermore, still due to a strong confinement of propagating SPPs in the core of TDPW (see Fig. 4), one can also find that the propagating properties of SPPs are mainly decided by the properties of the core of the TDPW itself, and are almost not affected by the properties of two side claddings of the TDPW. And thus, as FDTD results show that L_p increases with w_m to a maximum value and to a stable value (see Fig. 3g), and on the other hand, the maximum L_p is approximate to that of MDMW with the same t_d (see Fig. 3h), which is much smaller than the result of EIM. Figure 3g shows that the diminishing L_p with the decrease of w_m is due to the edge scatter of light by the Ag stripe. In a word, the contradiction between the results of FDTD and EIM, in regard to the dependence of L_p and w_b on w_m as t_d is fixed, is attributed to the strong localization of SPPs in the core of the TDPW, while this was neglected in the EIM analysis. Finally, as far as the practical utilization of the devices based on the TDPW in the future is concerned, the oxidization of Ag can inevitably decrease the properties of the devices. In order to avoid the oxidization of Ag, the Ag stripe can be covered with a very thin layer of SiO_2 (10~20 nm), which will nearly not affect the propagation properties of the TDPW.

With the strong confinement of propagating SPPs in the TDPW, some bending components are considered based on the straight waveguide. First, an oblique bending constructed with the TDPW, shown in Fig. 5a, is investigated. Figure 5b, c presents the dependence of bend transmission on bending angle (θ) for $\lambda = 635$ nm with a waveguide cross section of 70×60 nm^2, and for λ=1550 nm with a waveguide cross section of 70×80 nm^2. The transmission of the bend is obtained through the ratio between the $|E|^2$ integrals in the core of the waveguide with a distance of 0.5 μm after (P_{out}) and before (P_{in}) the bending junction (see Fig. 5a). For $\lambda = 635$ nm/1550 nm, it

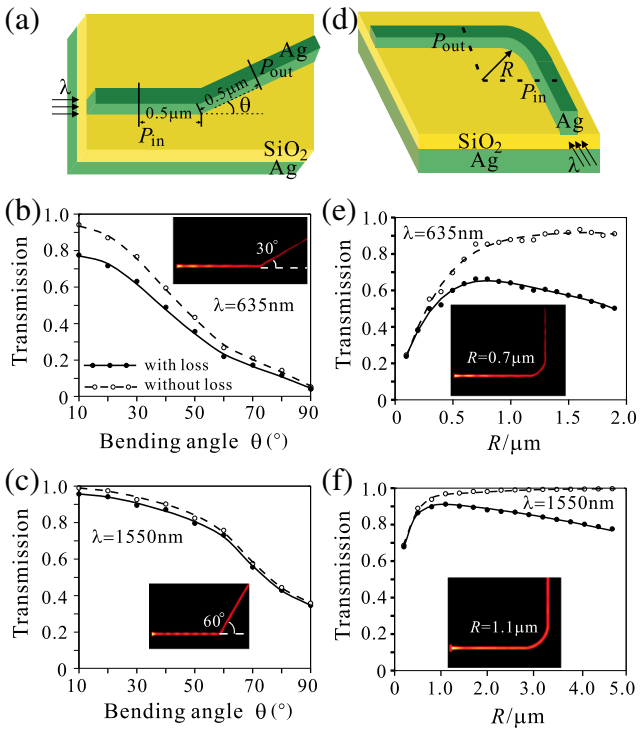

Fig. 5 Three dimensional schematics of **a** oblique bending and **d** 90° circular bending constructed with TDPW. FDTD results of dependence of bend transmission on bending angle (θ) for **b** $\lambda = 635$ nm and **c** $\lambda = 1550$ nm. FDTD results of dependence of bend transmission on R for **e** $\lambda = 635$ nm and **f** $\lambda = 1550$ nm, with **b**, **e** a waveguide cross section of 70×60 nm^2, and **c**, **f** with a waveguide cross section of 70×80 nm^2. Solid curve with solid circles for those with ohmic loss, and dashed curve with hollow circles for those without ohmic loss. The insets in **b**, **c**, **e**, **f** are FDTD-simulated electric field ($|E|^2$) distributions in the xy plane (color figure online)

can be noticed that when θ<30°/60°, the transmitted power decreases slowly with the bending angle θ, while the transmitted power declines rapidly when θ exceeds 30°/60°. And at θ=30°/60°, the transmittance is 63%/74%, with the distribution of $|E|^2$ shown in the inset of Fig. 5e, f.

Furthermore, a 90° circular waveguide bend with a radius of R structured with the TDPW is studied, as shown in Fig. 5d. Figure 5e, f exhibits the dependence of bend transmission on R for $\lambda = 635$ nm with a waveguide cross section of 70×60 nm^2, and for $\lambda = 1550$ nm with a waveguide cross section of 70×80 nm^2. The transmission of the bend is obtained through the ratio between the $|E|^2$ integrals in the core of the waveguide at the end (P_{out}) and at the beginning (P_{in}) of the bend section (see Fig. 5d). For $\lambda = 635$ nm, the real transmission (solid curve) shows that when R<0.7 μm, the transmission of the bend increases with R, and while $R > 0.7$ μm, the transmission decreases gradually. This is because a smaller bending radius R leads to a high radiative loss (see dashed curves, the transmission of the bend considering without ohmic loss); as R is increased, the ohmic loss is increased with the length of the bending. Thus, determined by the trade-off

between the radiative loss and ohmic loss, there exists an optimal radius $R = 0.7$ μm, reaching a maximum transmittance about 68%; the corresponding electric filed distribution is shown in the inset of Fig. 5e. Therefore, the optimal radius for 1550 nm is R=1.1 μm with the maximum transmittance of 91.3%, as the field distribution is shown in the inset of Fig. 5f. Moreover, surprisingly, due to the strong localization of SPPs in the TDPW, for $\lambda = 1550$ nm, the bend with a minimum R of 2.6 μm may realize a nearly zero radiation loss (see dashed curve in Fig. 5f), compared with the circular bend structured with dielectric-loaded plasmonic waveguide still with a radiation loss of near 10%, where the minimum $R$is at least 7 μm [23].

Conclusions

In conclusion, the authors propose a TDPW with a very simple structure, which is created by depositing an Ag stripe onto MDAW. By employing EIM analysis and FDTD simulations, we find that the propagation properties of the TDPW are mainly decided by the core itself, due to the much stronger localization of SPPs in the core than in the two side claddings. The SPPs propagating in the TDPW even with a very small waveguide cross section is strongly confined in the core and only extends a very small distance in the two side claddings. Besides, two bending waveguides, oblique bending waveguides and 90° circular bending waveguides, are also investigated. For $\lambda = 1550$ nm, the 90° circular bending with the smallest radius of 2.6 μm shows a nearly zero radiative loss, even in a small waveguide cross section of 70×80 nm^2. The proposed TDPW is suitable for planar integration, and will be useful for building various types of nanophotonic components and will find its applications in photonic integrated circuits.

Funding information This work is financially supported by the National Nature Science Foundation of China (Grant Nos. 61575145, 61205166, and J1210061).

Compliance with Ethical Standards

Conflict of Interest The authors declare that they have no competing interests.

References

1. Barnes W, Dereux A, Ebbesen T (2003) Surface plasmon subwavelength optics. Nature 424(6950):824–830. https://doi.org/10.1038/nature01937
2. Ozbay E (2006) Plasmonics: merging photonics and electronics at nanoscale dimensions. Science 311(5758):189–193. https://doi.org/10.1126/science.1114849
3. Gramotnev DK, Bozhevolnyi SI (2010) Plasmonics beyond the diffraction limit. Nat Photonics 4(2):83–91. https://doi.org/10.1038/nphoton.2009.282
4. Maier SA, Kik PG, Atwater HA, Meltzer S, Harel E, Koel BE, Requicha AAG (2003) Local detection of electromagnetic energy transport below the diffraction limit in metal nanoparticle plasmon waveguides. Nat Mater 2(4):229–232. https://doi.org/10.1038/nmat852
5. Dickson RM, Lyon LA (2000) Unidirectional plasmon propagation in metallic nanowires. J Phys Chem B 104(26):6095–6098. https://doi.org/10.1021/jp001435b
6. Weeber JC, Krenn JR, Dereux A, Lamprecht B, Lacroute Y, Goudonnet JP (2001) Near-field observation of surface plasmon polariton propagation on thin metal stripes. Phys Rev B 64(4):045411. https://doi.org/10.1103/PhysRevB.64.045411
7. Tanaka K, Tanaka M (2003) Simulations of nanometric optical circuits based on surface plasmon polariton gap waveguide. Appl Phys Lett 82(8):1158–1160. https://doi.org/10.1063/1.1557323
8. Veronis G, Fan S (2005) Bends and splitters in metal-dielectric-metal subwavelength plasmonic waveguides. Appl Phys Lett 87(13):131102. https://doi.org/10.1063/1.2056594
9. Kusunoki F, Yotsuya T, Takahara J, Kobayashi T (2005) Propagation properties of guided waves in index-guided two-dimensional optical waveguides. Appl Phys Lett 86(21):211101. https://doi.org/10.1063/1.1935034
10. Pile DFP, Ogawa T, Gramotnev DK, Matsuzaki Y, Vernon KC, Yamaguchi K, Okamoto T, Haraguchi M, Fukui M (2005) Two-dimensionally localized modes of a nanoscale gap plasmon waveguide. Appl Phys Lett 87(26):261114. https://doi.org/10.1063/1.2149971
11. Liu L, Han Z, He S (2005) Novel surface plasmon waveguide for high integration. Opt Exp 13(17):6645–6650. https://doi.org/10.1364/OPEX.13.006645
12. Wang B, Wang GP (2004) Metal heterowaveguides for nanometric focusing of light. Appl Phys Lett 85:3559–3601
13. Wang B, Wang GP (2007) Planar metal heterostructures for nanoplasmonic waveguides. Appl Phys Lett 90(1):013114. https://doi.org/10.1063/1.2430682
14. Wang B, Wang GP (2005) Simulations of nanoscale interferometer and array focusing by metal heterowaveguides. Opt Exp 13(26):10558–10563. https://doi.org/10.1364/OPEX.13.010558
15. Chen L, Wang B, Wang GP (2006) High efficiency 90 bending metal heterowaveguides for nanophotonic integration. Appl Phys Lett 89(24):243120. https://doi.org/10.1063/1.2404596
16. Kusunoki F, Yotsuya T, Takahara J (2006) Confinement and guiding of two-dimensional optical waves by low-refractive-index cores. Opt Express 14(12):5651–5656. https://doi.org/10.1364/OE.14.005651
17. Pile DFP, Gramotnev DK (2009) Channel plasmon–polariton in a triangular groove on a metal surface. Opt Lett 29:1069–1071
18. Bozhevolnyi SI, Volkov VS, Devaux E, Ebbesen TW (2005) Channel plasmon-polariton guiding by subwavelength metal grooves. Phys Rev Lett 95(4):046802. https://doi.org/10.1103/PhysRevLett.95.046802
19. Bozhevolnyi S, Volkov V, Devaux E, Laluet J, Ebbesen T (2006) Channel plasmon subwavelength waveguide components including interferometers and ring resonators. Nature 440(7083):508–511. https://doi.org/10.1038/nature04594
20. Moreno E, Rodrigo SG, Bozhevolnyi SI, Martín-Moreno L, García-Vidal FJ (2008) Guiding and focusing of electromagnetic fields with wedge plasmon polaritons. Phys Rev Lett 100:023901
21. Bian Y, Zheng Z, Zhao X, Liu L, Su Y, Zhu J, Zhou T (2013) Modal properties of triangular metal groove/wedge based hybrid plasmonic structures for laser actions at deep-subwavelength scale. Opt Commun 297:102–108. https://doi.org/10.1016/j.optcom.2013.01.075
22. Steinberger B, Hohenau A, Ditlbacher H, Stepanov AL, Drezet A, Aussenegg FR, Leitner A, Krenn JR (2006) Dielectric stripes on

gold as surface plasmon waveguides. Appl Phys Lett 88(9):094104. https://doi.org/10.1063/1.2180448
23. Krasavin AV, Zayats AV (2007) Passive photonic elements based on dielectric-loaded surface plasmon polariton waveguides. Appl Phys Lett 90(21):211101. https://doi.org/10.1063/1.2740485
24. Tsilipakos O, Yioultsis TV, Kriezis EE (2009) Theoretical analysis of thermally tunable microring resonator filters made of dielectric-loaded plasmonic waveguides. J Appl Phys 106(9):093109. https://doi.org/10.1063/1.3256139
25. Oulton RF, Sorger VJ, Genov DA, Pile DFP, Zhang ANDX (2008) A hybrid plasmonic waveguide for subwavelength confinement and long-range propagation. Nat Photonics 2(8):496–500. https://doi.org/10.1038/nphoton.2008.131
26. Chu HS, Li EP, Bai P, Hegde R (2010) Optical performance of single-mode hybrid dielectric-loaded plasmonic waveguide-based components. Appl Phys Lett 96(22):221103. https://doi.org/10.1063/1.3437088
27. Sorger VJ, Ye Z, Oulton RF, Wang Y, Bartal G, Yin X, Zhang X (2011) Experimental demonstration of low-loss optical waveguiding at deep sub-wavelength scales. Nat Commun 2:331. https://doi.org/10.1038/ncomms1315
28. Chu H, Bai P, Li E, Hoefer WRJ (2011) Hybrid dielectric-loaded plasmonic waveguide-based power splitter and ring resonator: compact size and high optical performance for nanophotonic circuits. Plasmonics 6(3):591–597. https://doi.org/10.1007/s11468-011-9239-y
29. Chu H, Akimov YA, Bai P, Li E (2011) Hybrid dielectric-loaded plasmonic waveguide and wavelength selective components for efficiently controlling light at subwavelength scale. J Opt Soc Am B 28(12):2895–2901. https://doi.org/10.1364/JOSAB.28.002895
30. Bian Y, Gong Q (2014) Highly confined guiding of low-loss plasmon waves in hybrid metal-dielectric slot waveguides. Nanotechnology 25(34):345201. https://doi.org/10.1088/0957-4484/25/34/345201
31. Zhang B, Bian Y, Ren L, Guo F, Tang S, Mao Z, Liu X, Sun J, Gong J, Guo X, Huang TJ (2017) Hybrid dielectric-loaded nanoridge plasmonic waveguide for low loss light transmission at the sub-wavelength scale. Sci Rep 7:40479. https://doi.org/10.1038/srep40479,1-9
32. Kaminow IP, Mammel WL, Weber HP (1974) Metal-clad optical waveguides: analytical and experimental study. Appl Opt 13(2):396–405. https://doi.org/10.1364/AO.13.000396
33. Johnson PB, Christy RW (1972) Optical constants of the noble metals. Phys Rev B 6(12):4370–4379. https://doi.org/10.1103/PhysRevB.6.4370